Nuclear envelope rupture is induced by actin-based nucleus confinement

Emily M. Hatch[1] and Martin W. Hetzer[2]

[1]Department of Basic Sciences, The Fred Hutchinson Cancer Research Center, Seattle, WA 98109
[2]Molecular and Cell Biology Laboratory, Salk Institute for Biological Studies, La Jolla, CA 92037

Repeated rounds of nuclear envelope (NE) rupture and repair have been observed in laminopathy and cancer cells and result in intermittent loss of nucleus compartmentalization. Currently, the causes of NE rupture are unclear. Here, we show that NE rupture in cancer cells relies on the assembly of contractile actin bundles that interact with the nucleus via the linker of nucleoskeleton and cytoskeleton (LINC) complex. We found that the loss of actin bundles or the LINC complex did not rescue nuclear lamina defects, a previously identified determinant of nuclear membrane stability, but did decrease the number and size of chromatin hernias. Finally, NE rupture inhibition could be rescued in cells treated with actin-depolymerizing drugs by mechanically constraining nucleus height. These data suggest a model of NE rupture where weak membrane areas, caused by defects in lamina organization, rupture because of an increase in intranuclear pressure from actin-based nucleus confinement.

Introduction

The nuclear envelope (NE) has been thought to be a static barrier during interphase. However, recent work demonstrated that both the nuclear lamina and the NE can undergo significant morphological changes during interphase (Hatch and Hetzer, 2014). One type of interphase NE dynamic is rupture and repair of the NE membrane, which results in a transient loss of nuclear integrity and mixing of cytosolic and nuclear components. Transient NE rupture has been observed after viral infection (de Noronha et al., 2001; Cohen et al., 2006), in cultured cancer and laminopathy cells (De Vos et al., 2011; Vargas et al., 2012; Maciejowski et al., 2015), and in cells migrating through small pores (Denais et al., 2016; Raab et al., 2016). Loss of nuclear integrity is, at least initially, not fatal to the cell; cells that undergo NE rupture do not have increased rates of apoptosis and divide normally (De Vos et al., 2011; Denais et al., 2016; Raab et al., 2016).

Interphase NE rupture is correlated with altered nuclear lamina organization and chromatin herniation. The nuclear lamina is an intermediate filament meshwork composed of two types of lamin proteins, the B type (LmnB1 and LmnB2) and the A type (LmnA/C), and associated inner nuclear membrane proteins (Gruenbaum et al., 2005). This network determines the mechanical properties and morphology of the nucleus (Gruenbaum and Foisner, 2015). Lesions in the LmnB1 network occur after some viral infections (de Noronha et al., 2001; Cohen et al., 2006), partial depletion of LmnB1 or expression of disease-associated LmnA/C mutants (Muchir et al., 2004; Dechat et al., 2010), and mechanical compression (Le Berre et al., 2012; Thiam et al., 2016). NE rupture occurs at these LmnB1 lesions (de Noronha et al., 2001; Cohen et al., 2006; De Vos et al., 2011; Vargas et al., 2012; Maciejowski et al., 2015; Denais et al., 2016; Raab et al., 2016), and repairing these defects by overexpressing LmnB1 or LmnB2 is sufficient to prevent NE rupture (Vargas et al., 2012; Hatch et al., 2013). Areas of the NE lacking LmnB1 often lack other lamina proteins and nuclear pore complexes and are frequently the site of chromatin herniation (Sullivan et al., 1999; de Noronha et al., 2001; Vigouroux et al., 2001; Muchir et al., 2004; Shimi et al., 2008). Thus, the current mechanism of NE rupture is that when LmnB1 lesions occur, they result in areas of weak membrane that are prone to rupture (De Vos et al., 2011; Tamiello et al., 2013; Hatch and Hetzer, 2014).

Cytoskeleton interactions with the nucleus also determine its morphology and mechanical properties. The linker of nucleoskeleton and cytoskeleton (LINC) complex, comprised of SUN (Sad1 and UNC-84) and KASH (Klarsicht, ANC-1, and Syne) domain–containing proteins, spans the NE and transmits force from microtubules and actin to the lamina (Starr and Fridolfsson, 2010). LINC complex interactions with microtubules via dynein can cause nucleus deformation and membrane ripping (Beaudouin et al., 2002; Salina et al., 2002). Interactions with actin can increase the density of contractile perinuclear actin bundles (Khatau et al., 2009; Lombardi et al., 2011; Lovett et al., 2013) and flatten the nucleus by compressing or confining

Correspondence to Martin Hetzer: hetzer@salk.edu

Abbreviations used: cytoD, cytochalasin D; LINC, linker of nucleoskeleton and cytoskeleton; MN, micronuclei; NE, nuclear envelope; PDMS, polydimethylsiloxane.

The Rockefeller University Press $30.00
J. Cell Biol. Vol. 215 No. 1 27–36
www.jcb.org/cgi/doi/10.1083/jcb.201603053

its height (Lovett et al., 2013). Increased actin assembly also causes increased chromatin herniation (Tamiello et al., 2013; Kanellos et al., 2015). Thus, there are several mechanisms by which cytoskeletal connections could promote NE instability.

Here we show that, in cultured cancer cells, NE rupture is inhibited by the loss of contractile actin bundles associated with the nucleus. Disruption of actin filaments, contractile actin fibers, or LINC complexes significantly impairs NE rupture. These conditions did not affect nuclear lamina organization, but did suppress the formation and growth of chromatin hernia. These data suggested that NE-associated actin bundles could be promoting NE rupture by constraining nucleus height. Supporting this idea, we found that NE rupture could be rescued in the absence of actin assembly by mechanically flattening the nucleus. This indicates that confinement of the nucleus is required, in addition to lamina disruption, to drive NE instability and that perinuclear actin bundles are the main source of this stress in cultured cells.

Results and discussion

We used a previously developed U2OS-based reporter cell line (U2OS GFP-NLS shLmnB1; Hatch et al., 2013) to study the mechanism of NE rupture during interphase. These cells express three GFPs fused to a nuclear localization signal (GFP-NLS) to assess nuclear integrity. Cytoplasmic accumulation of GFP-NLS indicates NE rupture, and repair is indicated by GFP-NLS reaccumulation in the nucleus (Fig. 1 A and Video 1; Anderson et al., 2009; De Vos et al., 2011; Vargas et al., 2012). The U2OS cells also express an shRNA against LmnB1 that decreases LmnB1 expression in the population to 60% of normal levels (Hatch et al., 2013). LmnB1 levels at the NE are reduced compared with control cells, and LmnA levels are unaltered (Fig. S1, A–C). This modest decrease in LmnB1 expression is sufficient to increase the frequency of both lamina disruption (Fig. S1 D) and NE rupture (Fig. S1 E).

To determine whether cytoskeleton interactions affected NE rupture or repair, we performed live-cell imaging of U2OS GFP-NLS shLmnB1 cells after drug treatment to depolymerize actin filaments or microtubules. To avoid off-target effects from mitotic phenotypes, we arrested cells in S phase before and during drug incubation (Fig. 1 B). We found that treatment with either cytochalasin D (cytoD) or latrunculin A, which block actin polymerization (Fig. S1 F), significantly inhibited NE rupture compared with the DMSO control (Fig. 1 C, Fig. S1 G, and Videos 2 and 3). Similar results were observed in HeLa cells (Fig. S1 H), indicating that this result is not cell-type specific. In contrast, incubation of U2OS cells in medium (Fig. 1 C) or high doses (Fig. S1 I) of nocodazole, which depolymerizes microtubules, did not inhibit NE rupture and slightly increased NE rupture at high doses.

To test whether actin filaments or higher-order actin assemblies were promoting NE rupture, we treated cells with blebbistatin, a myosin II inhibitor, to prevent the assembly of contractile actin bundles. Loss of actin bundles strongly inhibited NE rupture (Fig. 1 D and Video 4), similar to actin depolymerization, indicating that actin fiber assembly, rather than actin polymerization, is required for NE rupture.

We had previously observed that micronuclei (MN) in mammalian cells have a high probability of NE rupture (Hatch et al., 2013). We found that, in contrast to the primary nuclei, MN rupture does not require the actin cytoskeleton. The proportion of disrupted to intact MN was the same before drug addition and after 18-h incubation in DMSO or cytoD (Fig. 1, E and F).

To test whether the LINC complex was required for NE rupture, we first used siRNAs to deplete either Sun1 or Sun2, the two main SUN-domain–containing proteins in mammalian cells (Starr and Fridolfsson, 2010), in U2OS GFP-NLS shLmnB1 cells. siRNA transfection resulted in at least 90% knockdown of the targeted protein (Fig. 2 A), and immunofluorescence analysis confirmed that the knockdown was specific and that the targeted protein was lost from the NE (Fig. S2 A). We found that Sun1 depletion, but not Sun2 depletion, caused a significant inhibition of NE rupture compared with cells transfected with control siRNAs (Fig. 2 B). A separate siRNA against Sun1 (Sun1.2) also inhibited NE rupture, confirming the specificity of this result (Fig. S2, A–C).

Previous studies suggested that Sun1 and Sun2 have redundant functions in LINC complex assembly in human cells (Rothballer and Kutay, 2013). However, we found that only Sun1 depletion resulted in mislocalization of both mCherry-KASH1 (mCherry fused to the KASH domain from nesprin-1a) and endogenous nesprin2 (Nsp2) from the NE after detergent extraction (Fig. S2 D). These data suggest that Sun1 is the major interaction partner for KASH-domain proteins in U2OS nuclei and that Sun2 is not sufficient for LINC complex assembly.

To determine whether the requirement for Sun1 in NE rupture was because of its function in LINC complex assembly, we also assessed NE rupture after overexpressing mCherry-KASH1 to disrupt endogenous nesprin protein binding to Sun1. mCherry-KASH1 expression, but not mCherry alone, was sufficient to cause loss of coexpressed GFP-Nsp1 and endogenous Nsp2 from the NE after detergent extraction (Fig. 2 C and Fig. S2, E and F). These data indicate that KASH1, consistent with previous results (Lombardi et al., 2011), acts as a dominant negative and disrupts endogenous LINC complex assembly. Expression of mCherry-KASH1 significantly inhibited NE rupture compared with mCherry alone (Fig. 2 D). Together with the result that Sun1 depletion inhibits LINC complex assembly and NE rupture, these data indicate that LINC complex assembly is required for NE rupture.

We next asked which step in NE rupture was affected by the loss of actin bundles and whether the same step was affected by LINC complex disruption. To assess the effects of actin and LINC complex assembly on nuclear lamina organization, we quantified the level of lamina lesions in U2OS GFP-NLS shLmnB1 cells treated with blebbistatin or Sun1 siRNAs compared with control cells. The number of lamina lesions in each nucleus was estimated by quantifying the number of LmnA fragments in nuclear rim images. LmnA is frequently absent from lamina lesions generated by LmnB1 depletion (Vergnes et al., 2004; Shimi et al., 2008), and the presence of LmnA "fragments" at the rim correlates with the presence of lamina holes in surface scans (Fig. 3, A and C). We found that neither blebbistatin nor Sun1 depletion affected the mean number of lesions per nucleus compared with control cells (Fig. 3, B and D). In addition, neither blebbistatin nor Sun1 siRNAs affected LmnB1 or LmnA levels by Western blot (unpublished data). These data indicate that the inhibition of NE rupture by loss of actin or LINC complex assembly is not caused by repair of nuclear lamina lesions.

In contrast, we found that blebbistatin treatment and Sun1 knockdown reduced the appearance of chromatin

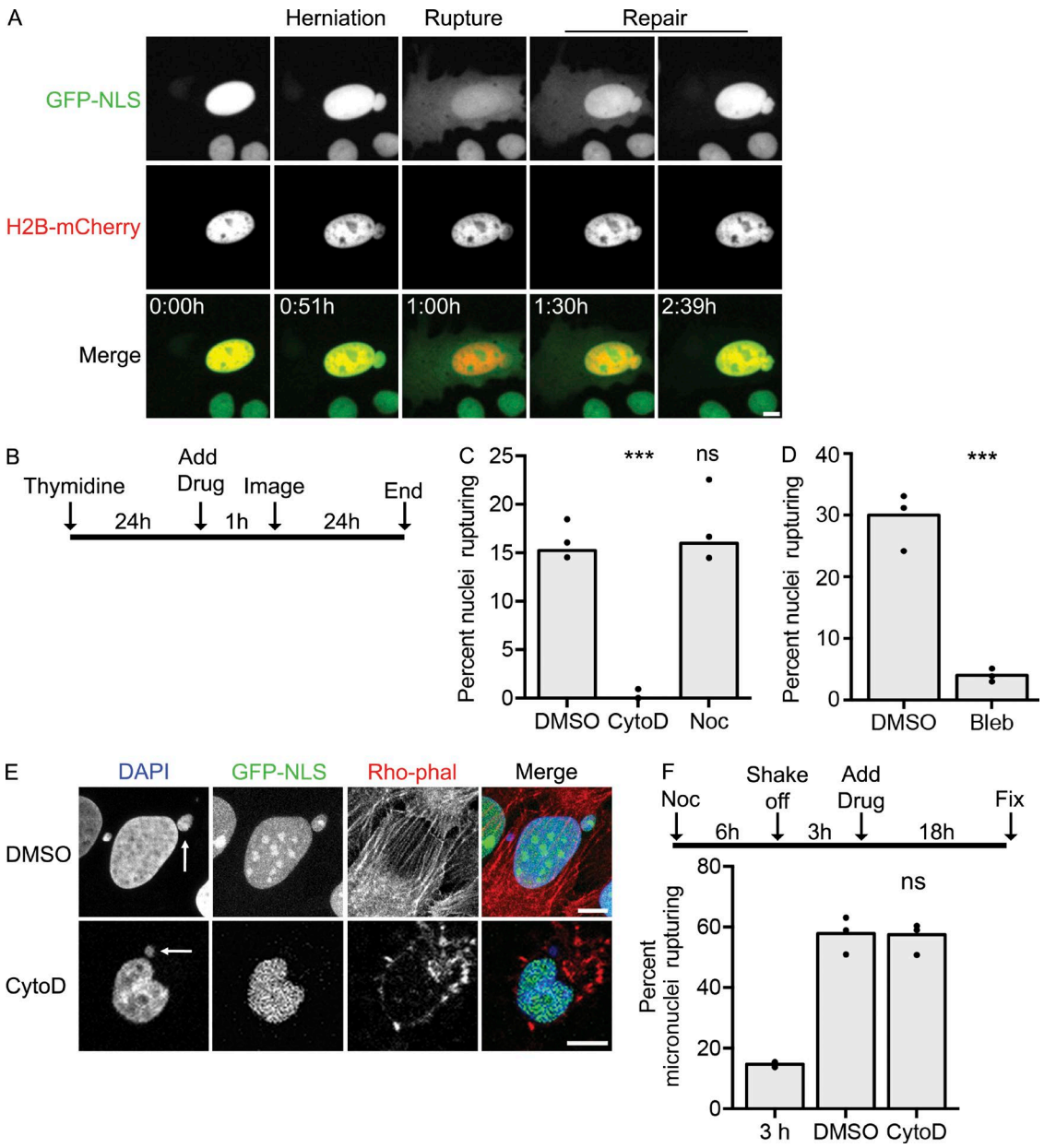

Figure 1. **Assembly of contractile actin bundles is required for interphase NE rupture in the primary nucleus.** (A) Still images from time-lapse imaging of U2OS cells expressing 3xGFP-NLS (GFP-NLS), histone 2B (H2B)-mCherry, and LmnB1 shRNA. Chromatin herniation is indicated by localization of H2B-mCherry and GFP-NLS to a nucleus bleb. NE rupture is indicated by GFP-NLS localization to the cytoplasm. NE repair is indicated by GFP-NLS reaccumulation in the nucleus. Time in hours:minutes. (B) Experiment schematic for time-lapse imaging of NE rupture in U2OS GFP-NLS shLmnB1 cells. (C and D) Quantification of NE rupture after treatment with indicated drugs. Graph represents pooled data (columns) from 3 experiments (points, $n > 200$ cells/expt.). ***, $P < 0.001$; ns, $P > 0.05$, Fisher's exact test. Bleb, blebbistatin; CytoD, cytochalasin D; Noc, nocodazole. (E) Representative images of micronuclei (arrows) in cells treated for 18 h with indicated drugs and labeled with rhodamine-phalloidin (rho-phal) to visualize F-actin. The micronucleus in the top image is intact and the bottom one is disrupted. (F) Experiment schematic (top) for analysis of micronucleus disruption. Quantification (bottom) of disrupted micronuclei frequency 3 h after cell replating and 18 h after addition of indicated drug. Graph represents pooled data (columns) from three independent experiments (points, $n > 100$ cells). ns, $P > 0.05$, Fisher's exact test. Bars, 10 µm.

herniations (Fig. 3, E and H). Quantification of live-cell imaging data showed that both the number (Fig. 3, F and I) and size (Fig. 3, G and J) of chromatin hernia were reduced after disruption of contractile actin bundles or LINC complexes. In addition, we observed regression of existing hernia in cells treated with blebbistatin (Video 5). These data demonstrate that contractile actin bundles and the LINC complex function at the same step in NE rupture and that actin cytoskeleton interactions with the LINC complex promote the distension of the nuclear membrane and chromatin at the site of lamina lesions.

Two models for how LINC complex interactions with actin bundles could affect chromatin hernia frequency are (1) interactions at the sites of lamina lesions pull the membrane and chromatin away from the nucleus or (2) interactions all around the nucleus increase perinuclear actin bundle density and cause nucleus flattening, which drives chromatin herniation (Le Berre et al., 2012; Tamiello et al., 2013). The first model requires that

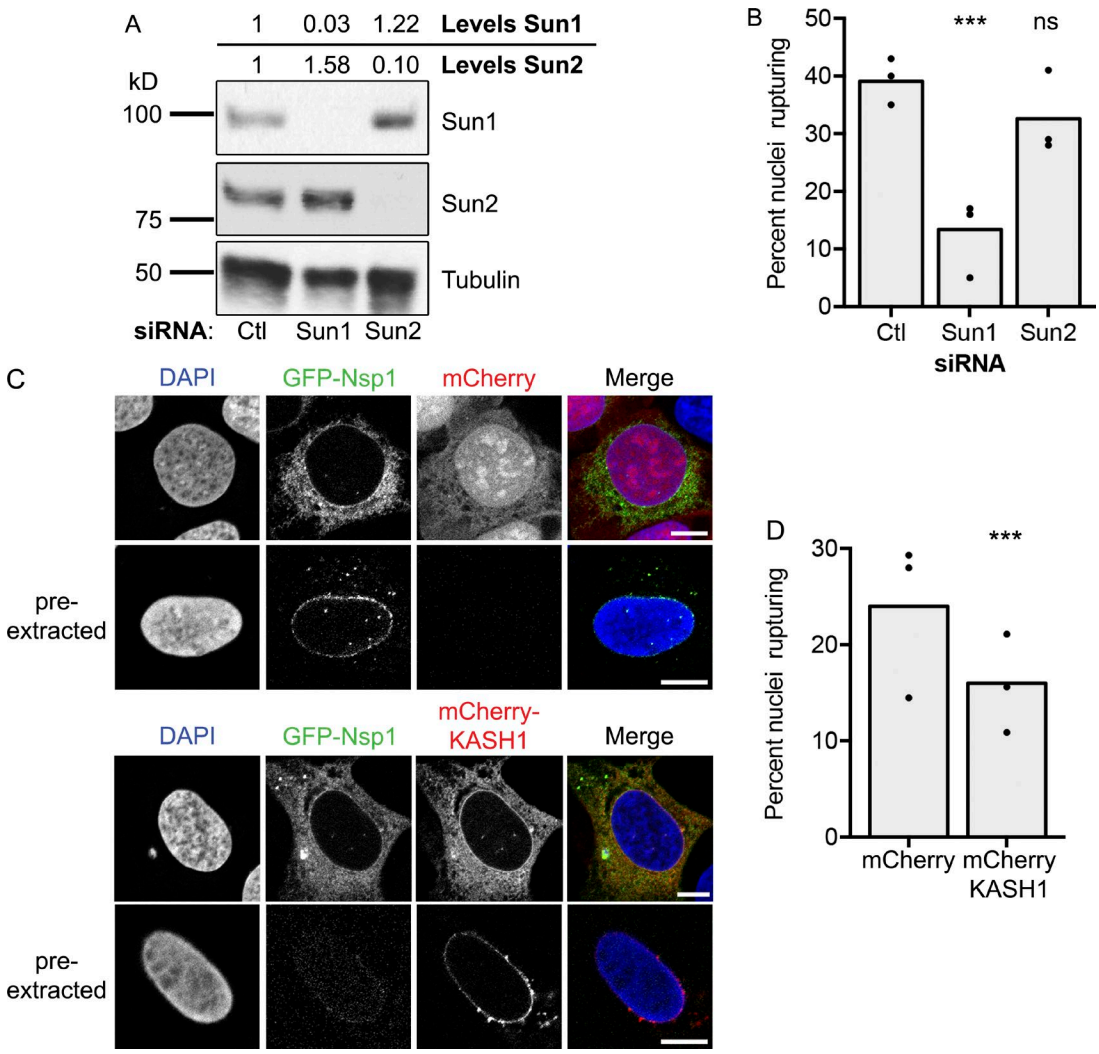

Figure 2. **The LINC complex is required for interphase NE rupture.** (A) Western blot of U2OS GFP-NLS shLmnB1 lysates after transfection with indicated siRNAs. Antibodies used are listed at right. Protein levels are mean values from four Western blots. (B) Quantification of NE rupture after transfection of indicated siRNAs. Graph represents pooled data (columns) from three independent experiments (points, $n > 100$ cells). ns, $P > 0.05$; ***, $P < 0.001$, Fisher's exact tests versus control. (C) Representative images of U2OS cells cotransfected with GFP-Nsp1 and mCherry-KASH1 or mCherry alone. Cells were pre-extracted with detergent before fixation in the bottom panels. (D) Quantification of NE rupture after transfection with indicated construct. Graph represents pooled data (columns) from three independent experiments (points, $n > 75$ cells). ***, $P < 0.001$, Fisher's exact test. Bars, 10 µm.

LINC complexes localize to chromatin hernia and the membrane at lamina lesions. Analysis of LINC complex localization by immunofluorescence showed that Sun1, Sun2, Nsp1, and Nsp2 are all absent from lamin-free areas of the NE (Fig. 4), suggesting that the first model is incorrect.

In support of the second model, and consistent with previous data (Khatau et al., 2009), perinuclear actin bundles, specifically the apical actin fibers, were disrupted by treatment with cytoD, blebbistatin, or Sun1 siRNAs compared with control cells and cells treated with nocodazole or Sun2 siRNAs (Fig. S1 F and Fig. S3 A). Next, nucleus flattening was analyzed by quantifying nucleus confinement in the z-direction (nucleus height). U2OS GFP-LmnB1 cells were treated with cytoskeleton drugs or Sun protein siRNAs and the distance between the top and bottom nuclear lamina sheets in z-projections was measured. As expected (Khatau et al., 2009; Chancellor et al., 2010; Versaevel et al., 2012), conditions that disrupted perinuclear actin bundles also increased nucleus height (Fig. S3, B–D). Sun2 depletion caused a significant increase in nucleus height even though perinuclear actin bundles are present. However, this was accompanied by an increase in volume (Fig. S3 E), suggesting that height is not indicative of nucleus confinement in this case. These data suggest that NE rupture is caused by nucleus confinement from perinuclear actin bundles.

To test whether nucleus confinement is sufficient to drive NE rupture, we used a microfabricated device to mechanically restrict cell and nucleus height in the absence of actin polymerization. A glass coverslip bonded to an array of 4.4-µm polydimethylsiloxane (PDMS) pillars was placed on top of a PDMS column and inverted on top of the cells (Fig. 5 A), as previously described (Le Berre et al., 2014). Cells in the area under the coverslip but between the pillars (Fig. 5 B, white circles) are thus confined to approximately the height of the pillars. Analysis of nucleus height showed that both DMSO- and cytoD-treated cells were confined to the same height and that this height was slightly smaller than unconfined, DMSO-treated cells and significantly smaller than cytoD-treated cells (Fig. 5, B and C). Nucleus confinement had no effect on actin

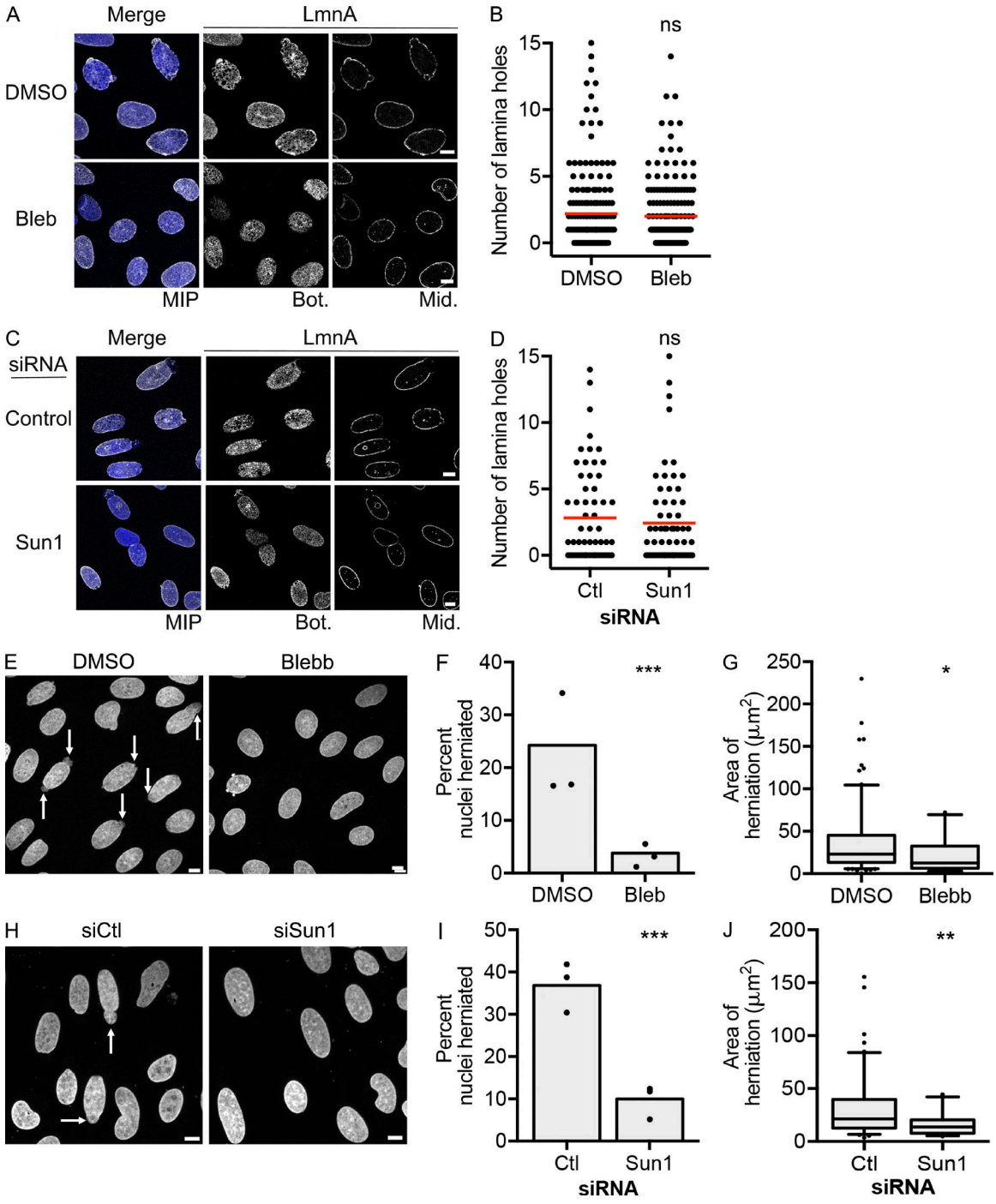

Figure 3. **Disruption of actin or LINC complexes decreases chromatin herniation without rescuing lamina disorganization.** (A) Representative images of U2OS GFP-NLS shLmnB1 cells arrested with thymidine, treated with indicated drugs, and labeled with DAPI and lamin A antibodies (LmnA). Bot., bottom section of nuclear lamina; Mid., midsection of nucleus rim used for analysis; MIP, maximum intensity projection of 11 and 12 sections with 0.55-µm step size. (B) Quantification of lamina holes in each nucleus rim. $n > 160$ cells from two experiments. Ns, $P > 0.05$, Mann–Whitney test. (C) Representative images of U2OS GFP-NLS shLmnB1 cells treated with indicated siRNAs, arrested with thymidine, and labeled with DAPI and LmnA antibodies. MIPs = 13 and 15 sections with 0.55-µm step size. (D) Quantification of lamina holes in each nucleus rim. $n > 60$ cells from three experiments. Ns, $P > 0.05$, Mann–Whitney test. (E) MIPs of DAPI-labeled cells arrested with thymidine and treated with indicated drugs (11 and 13 sections with 0.55-µm step size). Arrows indicate chromatin herniations. (F) Quantification of chromatin hernia formed during 24-h time-lapse imaging. Graph represents pooled data (columns) from three experiments (points, $n > 120$ cells). ***, $P < 0.001$, Fisher's exact test. (G) Quantification of maximum area of chromatin herniations present or emerging during 24-h time-lapse imaging. Boxes are quartiles and whiskers are 5th to 95th percentiles. $n = 160$ DMSO, 22 blebbistatin nuclei from three experiments. *, $P < 0.05$, Mann–Whitney test. (H) MIPs of DAPI labeled cells arrested with thymidine and treated with indicated drugs (12 and 14 sections with 0.42-µm step size). Arrows indicate chromatin herniations. (I) Quantification of chromatin hernia formed during 24-h time-lapse imaging. Graph represents pooled data (columns) from three experiments (points, $n > 80$ cells). ***, $P < 0.001$, Fisher's exact test. (J) Quantification of maximum area of chromatin herniations present or emerging during 24-h time-lapse imaging. $n = 110$ control and 33 Sun1 nuclei from three experiments. *, $P < 0.05$, Mann–Whitney test. Bars, 10 µm.

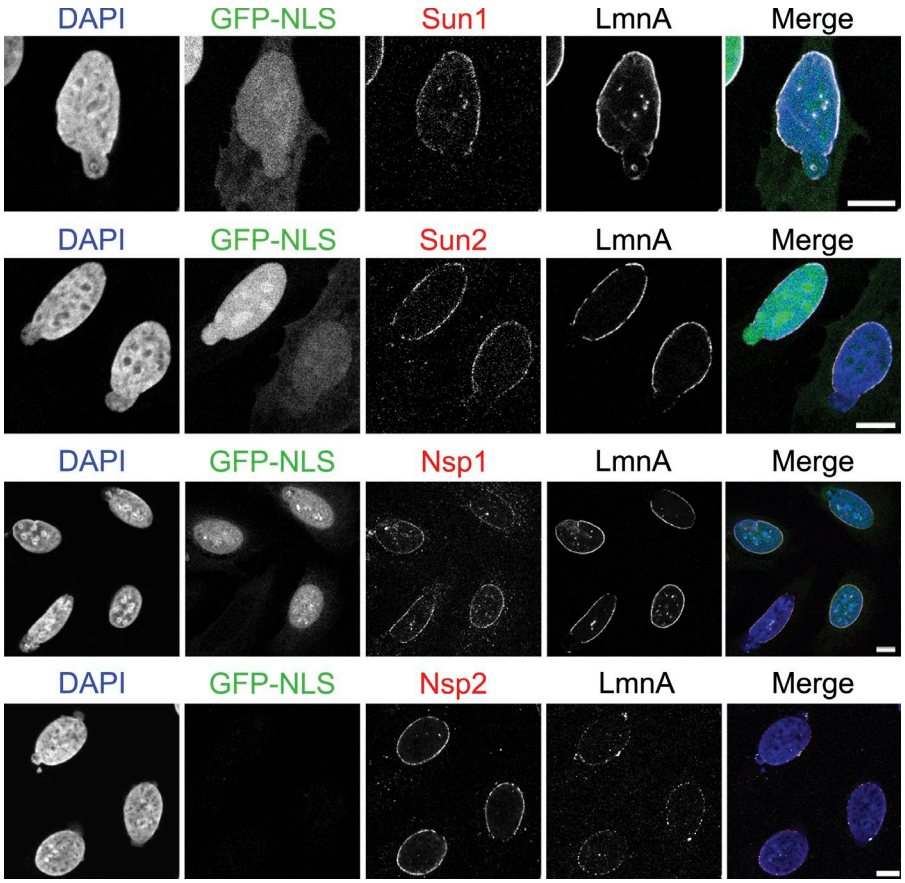

Figure 4. **The LINC complex is absent from chromatin hernia.** Representative images of U2OS GFP-NLS shLmnB1 cells arrested with thymidine, fixed, and labeled with LmnA antibodies (top three rows, rabbit; bottom, mouse) and (from top to bottom) Sun1, Sun2, nesprin1 (Nsp1), and nesprin2 (Nsp2) antibodies. Bars, 10 µm.

assembly in either the cytoplasm or the nucleus of cytoD-treated cells (Fig. S3 f). We first asked whether confinement increased chromatin herniation. Time-lapse observation of confined and unconfined DMSO- and cytoD-treated cells demonstrated that confinement causes a significant increase in chromatin hernia frequency in both drug conditions and rescues the loss of chromatin herniation in cytoD-treated cells (Fig. 5, D and E). Next, we analyzed NE rupture and found that confinement increased the frequency of NE rupture in both drug conditions and rescued the inhibition of NE rupture after cytoD treatment (Fig. 5 F and Videos 6 and 7). Similar results were also observed after confinement of DMSO- and cytoD-treated HeLa GFP-NLS cells (Fig. S3 G). These data indicate that the actin cytoskeleton itself is not required for NE rupture but that confinement of the nucleus promotes NE rupture in multiple cell types.

Our data support a model according to which interphase NE rupture occurs when lamin disorganization generates lamin-free weak areas on the NE. These areas are prone to both chromatin herniation and NE rupture when external force on the nucleus, such as actin-based nucleus compression or stretching, increases the stress on the membrane (Fig. 5 G). Although chromatin herniation is not required for NE rupture (Video 1, top left, at $t = 8$ s), our data suggest that the longevity of chromatin herniations correlates with the frequency of NE rupture in single cell. Consistent with previous results (Le Berre et al., 2012), chromatin herniations appear to persist longer in mechanically confined cells and correlate with increased NE rupture frequency per nucleus (compare Video 6 to Video 2). In contrast, mechanical confinement does not appear to affect the timing of GFP-NLS reaccumulation in the nucleus after NE rupture (Video 6; compare with Video 2). Together, these data suggest that NE membrane repair and chromatin hernia repair are not coordinated and that only the latter process is affected by the amount of stress on the nucleus.

Our conclusion that NE rupture in cultured cells results from increased stress on the nucleus is consistent with other examples of NE rupture in vitro and in vivo. Recent observations of dendritic cells, fibroblasts, and cancer cells migrating through small pores in vitro and in vivo demonstrated that NE rupture occurs at the leading end of the nucleus and coincides with extensive nucleus constriction (Denais et al., 2016; Raab et al., 2016). In addition, NE rupture is also observed when chromatin bridges exert a pulling force on the nucleus (Maciejowski et al., 2015). We did not find a link between actin cytoskeleton–based compression and NE rupture in MN. However, this does not rule out membrane tension from other mechanisms as a triggering event.

Transient NE rupture has significant consequences for the nucleus, including altered gene expression (De Vos et al., 2011), increased DNA damage (Denais et al., 2016; Raab et al., 2016), and chromothripsis (Maciejowski et al., 2015). Our data support a model where, when the nucleus is under stress in vivo (e.g., during cell migration or muscle contraction), it is more likely to lose integrity and to have increased levels of genome instability, especially when the nuclear lamina is already disrupted. Because altered NE structure is characteristic of many cancers and laminopathies, we believe that NE rupture could be an important contributor to cellular dysfunction in these diseases.

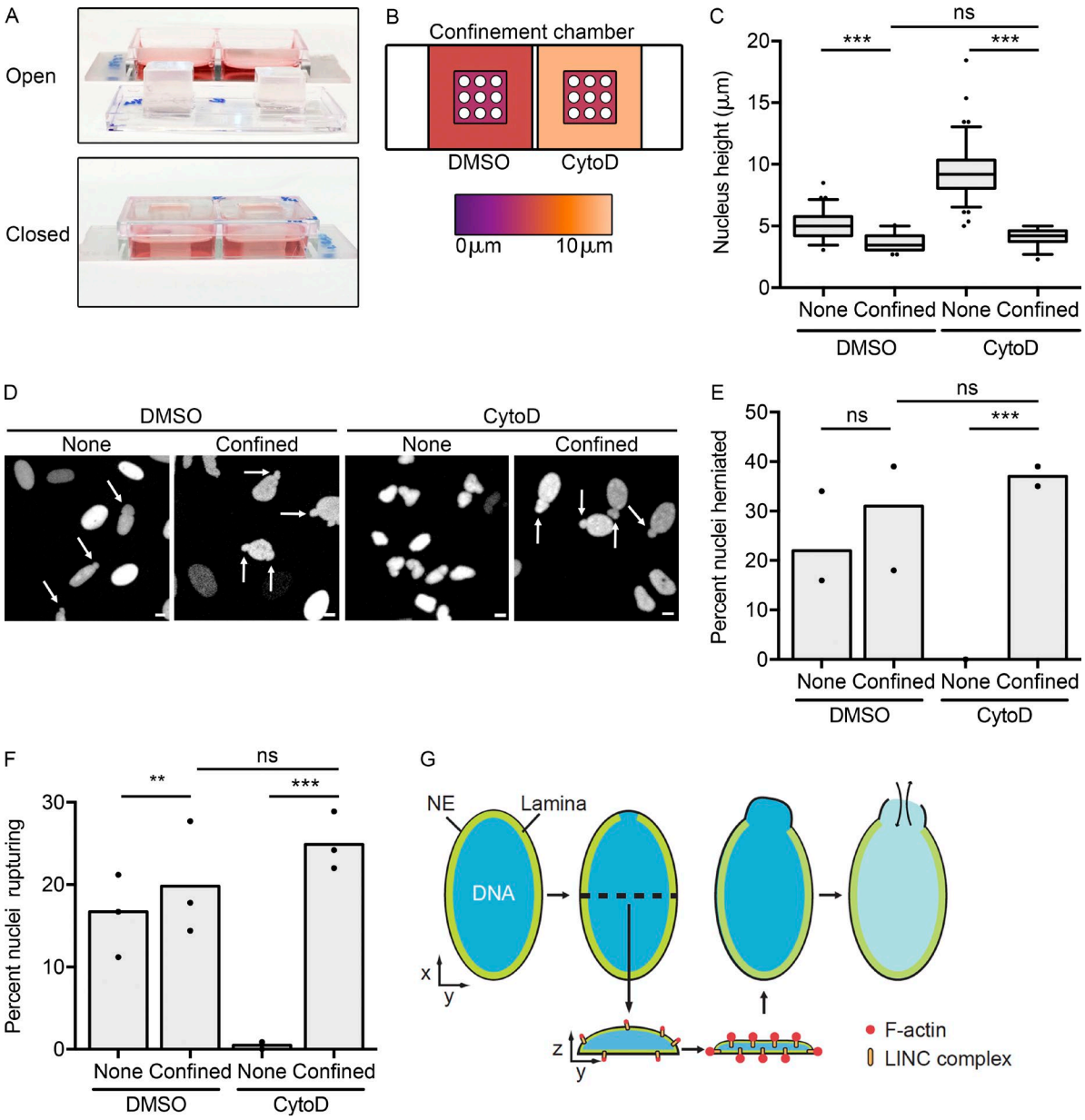

Figure 5. **Mechanical confinement of U2OS nuclei is sufficient for NE rupture.** (A) Images of cell confinement device. (B) Schematic representation of confinement device as viewed from objective. Large squares represent wells, small squares represent areas under the confinement slide, and circles indicate areas where pillars contact well bottom (not to scale). Colors represent mean nucleus height from C. (C) Quantification of nucleus height of U2OS GFP-LmnB1 cells treated with indicated drugs and confined for at least 1 h before imaging. Boxes are quartiles and whiskers are 5th to 95th percentiles. $n \geq 60$ nuclei; two-way analysis of variance, $P < 0.001$ for drug and confinement variables. **, $P < 0.01$; ***, $P < 0.001$ (multiple comparisons). (D) Images from 24-h time lapse of U2OS GFP-NLS shLmnB1 cells confined after treatment with indicated drugs. Arrows indicate sites of chromatin herniation. (E) Quantification of chromatin hernia formed during 24-h time-lapse imaging. Graph represents pooled data (columns) from two experiments (points, $n > 150$ cells). χ^2 analysis $P < 0.001$, results of Fisher's exact test between indicated pairs above the graph. ***, $P < 0.001$; ns, $P > 0.05$. (F) Quantification of NE rupture during 24-h time-lapse imaging. Graph represents pooled data (columns) from three experiments (points, $n > 150$ cells). χ^2 analysis, $P < 0.001$, with results of Fisher's exact test between indicated pairs shown above the graph. **, $P < 0.01$; ***, $P < 0.001$; ns, $P > 0.05$. (G) Model of interphase NE rupture in cultured cells. Bars, 10 µm.

Materials and methods

Cell lines and transfection

U2OS and HeLa cells were grown in DMEM plus 10% FBS at 10% CO_2. Plasmids were transfected using Lipofectamine 2000 (Thermo Fisher Scientific) and siRNAs were transfected using siLentfect (Bio-Rad Laboratories) according to the manufacturer's instructions. Cells were not analyzed until at least 24 h after transfection. For time-lapse imaging, U2OS cells were arrested in S phase by a single addition of 2 mM thymidine 24 h before imaging and for the duration of imaging. HeLa cells were arrested in S phase by a single addition of 2 mM hydroxyurea. CytoD (Tocris Bioscience) was used at 1 µg/ml, blebbistatin (Sigma-Aldrich) was used at 50 µM, and latrunculin A (EMD Millipore) was used at 1 µM. Nocodazole (Sigma-Aldrich) was used at 0.1 µg/ml except where noted in the figure legend. For experiments on micronuclei, U2OS cells were incubated in 0.1 µg/ml nocodazole for 6 h, synchronized by mitotic shake off, and replated onto glass coverslips in fresh medium.

U2OS GFP-NLS cells were made by transfecting U2OS cells with 3xGFP-NLS, selecting with 0.5 mg/ml G418 for 2 wk, and collecting the GFP+ population by FACS. Lamin B1 was depleted in U2OS GFP-NLS cells by infection with a lentivirus containing PLKO.1:shRNA-LmnB1.71 (NM_005573.2-1258s1c1; Sigma-Aldrich), and selection with puromycin (Corning) at 2 µg/ml. The sequence of the lamin B1 shRNA is 5′-CCGGGCATGAGAATTGAGAGCCTTTCTCGAGAA AGGCTCTCAATTCTCATGCTTTTT-3′. HeLa GFP-NLS cells were made by infecting HeLa cells with retrovirus made from pQCXIB-3xGFP-NLS, selecting with 2 µg/ml puromycin, and collecting GFP-positive cells by FACS. U2OS GFP-NLS H2B-mCherry cells were made by cotransfecting U2OS cells with pIRESneo3:H2B-mCherry and pIRESpuro3:GFP-IBB plasmids, selecting with 50 µg/ml G418 (Corning) and 2 µg/ml puromycin, and collecting double positives by FACS. U2OS GFP-LmnB1 cells were purchased from Sigma-Aldrich (catalog 39252).

Plasmids and siRNAs

p3xGFP-NLS (GFP-NLS) was previously described (Vargas et al., 2012) and contains EGFP-NLS (PPKKKRKV)-EGFP in the Gateway vector pcDNA-DEST53. pIRESneo3:H2B-mCherry and pIRESpuro3: GFP-IBB were gifts of D. Gerlich (Institute of Molecular Biotechnology of the Austrian Academy of Sciences, Vienna, Austria; Steigemann et al., 2009; Schmitz et al., 2010). pEGFP-C1:Nesprin1a (GFP-Nsp1) was a gift from J. Lammerding (The Weill Institute for Cell and Molecular Biology, Cornell Univeristy, Ithaca, NY; Lombardi et al., 2011). The mCherry plasmid (pmCherry-C1) was made by cutting EGFP out of pEGFP-C1 (Takara Bio Inc.) with AgeI and BglII and ligating in a PCR of mCherry from pIRESneo3:H2B-mCherry cut with the same. pmCherry-C1:KASH1 (mCherry-KASH1) was made by digesting pmCherry-C1 with EcoRI and BamHI and ligating in Nsp1-KASH PCR from pCDH-EF1-MCS1-puro-mCherry-Nesprin-1αKASH (a gift from J. Lammerding; Lombardi et al., 2011) and cut with same. pQCXIB-GFP-NLS was made by PCRing 3xGFP-NLS from p3xGFP-NLS and annealed using SLIC cloning into pQCXIB (a gift from E. Campeau; Campeau et al., 2009; plasmid 17487; Addgene) cut with EcoRV.

siRNAs against Sun1 (Talamas and Hetzer, 2011) and Sun2 were ordered from Thermo Fisher Scientific with the following sequences: Sun1.1, 5′-CCAUCCUGAGUAUACCUGUCUGUAUDT DT-3′; Sun1.2, 5′-ACCAGGUGCCUUCGAAADTDT-3′; and Sun2, 5′-GCAGAAAGAAGGUGUGAUUDTDT-3′. An siRNA against luciferase (5′-UAUGCAGUUGCUCUCCAGCDTDT-3′) was used as a control. siRNAs were diluted to 100 nM in transfection medium and left on for 4 h. U2OS cells were transfected twice with siRNAs, 48 h apart, before analysis.

Immunofluorescence

For indirect immunofluorescence, U2OS cells were grown on glass coverslips and fixed in 4% paraformaldehyde in PBS for 10 min at RT. Pre-extracted cells were incubated in 0.1% NP-40 in 1xPBS for 5 min at RT before fixation. Tubulin and Nsp1 immunofluorescence was performed on cells fixed 10 min in methanol at −20°C and rehydrated 10 min in PBS at RT. Coverslips were blocked in 3% BSA in PBS plus 0.1% Triton X-100 for 30 min at RT and incubated in primary and secondary antibodies diluted in blocking buffer for 30 min each at RT. Coverslips were then briefly incubated in 1 µg/ml DAPI in PBS (Roche) and mounted in Vectashield (Vector Laboratories).

Antibodies used for immunofluorescence were: goat anti–lamin B1 (1:500; Santa Cruz Biotechnology, Inc.), rabbit anti–lamin A (1:500; Sigma-Aldrich), mouse anti–lamin A/C (131C3, 1:200; Thermo Fisher Scientific; Fig. 4, bottom), rabbit anti-Sun1 (1:200; Novus Biologics), rabbit anti-Sun2 (EPR6557, 1:100; Genetex), mouse anti nesprin1 [MANNES1A] (1:50, Thermo Fisher Scientific), and rabbit anti–nesprin 2 (SYNE2, 1:50; Sigma-Aldrich). Secondary antibodies conjugated to Alexa Fluor 488, 568, or 647 (Thermo Fisher Scientific) were used at 1:2,000. Rhodamine phalloidin (Thermo Fisher Scientific) was used at 1 U/ml and added to coverslips for 20 min at RT. For immunofluorescence experiments using two rabbit antibodies (Fig. 4; Sun1 and Sun2), coverslips were blocked after incubation in the first rabbit primary antibody in 20 µg/ml (in PBS + 3% BSA + 0.1% Triton X-100) goat anti–rabbit Fab fragment (Jackson ImmunoResearch Laboratories, Inc.) for 30 min at RT and then incubated in donkey anti–goat secondary conjugated to Alexa Fluor 568. The coverslips were then incubated in the second rabbit primary antibody followed by donkey anti rabbit secondary conjugated to Alexa Fluor 647. Controls were performed to ensure that antibody labeling was specific.

Most fixed samples and all live-cell z-stacks were imaged on a scanning confocal microscope (LSM 710; ZEISS) with a 63× 1.4 NA oil-immersion or a 40× 1.3 NA oil-immersion objective with Zen software (ZEISS). Fixed samples in Fig. S1 A; Fig. S2, A (Sun1.2), D (Nsp2), and F; and Fig. 4 (Nsp1 and Nsp2) were imaged on an SPE scanning confocal microscope (Leica Biosystems) with a 63× 1.4 NA oil immersion objective with Application software X (Leica Biosystems). Images are single confocal sections except where noted. Images were adjusted for brightness and contrast using ImageJ (Abràmoff et al., 2004) or Photoshop CS3 (Adobe).

Time-lapse imaging

Cells were plated into eight-well µ-slide chambers (Ibidi) and imaged on a ZEISS Axioscope/Yokagawa X1 spinning-disk confocal microscope with a 20× 0.8 NA air objective at 37°C and 10% CO_2 for most experiments. For experiments reported in Figs. S3 G, S2 C, and 1 G, cells were imaged on an Ultraview spinning disk system (PerkinElmer). Acquisition was performed on a Ti inverted microscope stand (Nikon) with Perfect Focus, fitted with a Plan Apochromatic 20×/0.75 dry objective (Nikon). Images were recorded on an ImagEM EMCCD camera cooled to −69°C (Hamamatsu Photonics). Cells were maintained at 37°C and 5% CO_2 on a Chamlide stage top incubator (Live Cell Instrument) for the duration of the experiment. Videos were cropped and adjusted for brightness and contrast using ImageJ and Photoshop. Cytoskeleton drugs were added at least 1 h before imaging. For confinement slide imaging, cells were plated in a two-well glass-bottom µ-slide (Ibidi), arrested in S phase for 24 h, treated with drug for 2 h, and confined for 1 h before imaging.

Western blots

Antibodies used for immunoblotting were as follows: mouse antitubulin (1:5,000; Sigma-Aldrich), mouse anti-GAPDH (1:5,000; Genetex), rabbit anti-Sun1 (1:1,000; Novus Biologicals), and rabbit anti-Sun2 (1:1,000; Genetex). Alexa Fluor 680– or 800–conjugated secondary antibodies (Thermo Fisher Scientific) were used at 1:10,000. Primary and secondary antibodies were incubated on Western blots for 1 h each. Western blot bands were quantified using a fluorescent imager (Odyssey; LI-COR Biosciences) and ImageJ. The integrated density of the bands was background subtracted and normalized to tubulin or GAPDH before comparison.

Statistics and quantification

Prism5 (GraphPad) was used to generate all graphs and perform statistical analyses. To determine whether the frequency of NE rupture in two or more cell populations was significantly different, we used Fisher's exact (for a 2 × 2 table) or χ^2 analysis on each experiment to obtain p-values with the null hypothesis that all populations had the same proportions. p-values were calculated for each replicate and if the

p-values were homogenous between replicates, and then the raw data were pooled and a final p-value calculated. χ^2 and Fisher's exact analyses were also used to analyze two-variable binary data (Fig. 5, E and F; and Fig. S3 G). Although this precluded analysis of the interaction between the two variables, it allowed us to analyze the full numerical counts in each dataset instead of working only with the averages of the experimental replicates.

Analysis of lamin A and B1 levels at the nuclear rim was performed as described in (Hatch et al., 2013). In brief, images of U2OS GFP-NLS and U2OS GFP-NLS shLmnB1 nuclear rims were acquired with matching acquisition parameters. Analysis was based on a previously described method (Hoffman et al., 2001) and began by selecting the chromatin area based on DAPI or GFP-NLS labeling and converting it to a three- to five-pixel border around the rim and measuring the area (A_I) and integrated density of fluorescence (F_I) of the selection for both LmnB1 and LmnA labeling using Photoshop. The area of selection was then expanded by at least two times and a second group of area and fluorescence measurements taken (A_O and F_O). The background subtracted fluorescent intensity values were obtained using the following formula: $F_I - [(F_O - F_I)/(A_I/A_O)] = F_{\_N}$.

For analysis of lamina lesions, cells were fixed with paraformaldehyde and labeled with antibodies against lamin A (rabbit). Analysis was performed in ImageJ on a section where the entire nuclear rim was in focus, selected from a 0.5-µm-step z-series. First, the DAPI or GFP-NLS image was thresholded to select each nucleus in the image. Second, each nucleus area selection was converted to a line 20 pixels wide. Third, the "straighten" command was used to convert each nuclear rim into a rectangular image. Fourth, the LmnA signal in these rim images was thresholded to quantify the number of rim objects. Objects inside the nucleus were excluded from the count. The number of lesions was calculated as the number of LmnA objects − 1. This method is a conservative count of the number of nuclei with lamina lesions because if the nucleus has one lamina lesion that is randomly placed at the ends of the rectangular image, then it will seen as having only one lamina object and no lesions.

Nucleus heights were measured by analyzing maximal z-distance between top and bottom LmnB1 signal in the plane of the longest nucleus axis in Zen (ZEISS). Nucleus volumes were measured from DAPI-labeled z-stack images. Nuclei were rendered using the surfaces function in Imaris v8.2 (BitPlane) and the volume of the rendering reported.

Microfabrication of confinement slide and chamber setup

The method described previously (Le Berre et al., 2012, 2014) to fabricate a geometrical confinement slide and multiwell confiner was followed with some modifications. The mold for the micropillar structures was fabricated using standard photolithography protocols on a silicon wafer using SU-8 2005 photoresist (MicroChem) spin coated onto the wafer such that the feature height = 4.4 µm, as determined by a Dektak XT Stylus Profilometer (Bruker Corporation). The mold was silanized before PDMS (GE Healthcare) slide pouring. A 9 × 9–mm coverglass was used instead of a 10-mm circular glass as a substrate for the PDMS confinement slide. Soft confinement pillars were made in a two-well glass-bottom µ-slide (ibidi) and cut into 9 × 9–mm square-bottom prisms and stuck without additional adhesive to the middle of the chamber lid. After a confinement slide was placed atop the pillar, the lid and pillar was soaked in culture medium for 1 h at 37°C, 10% CO_2 before use. During cell confinement and imaging, the lid was taped shut to maintain constant pressure on the cells.

Online supplemental material

Fig. S1 shows the characterization of U2OS shRNA-LmnB1 GFP-NLS cell line and cytoskeleton controls. Fig. S2 shows the results of Sun 1 depletion or overexpression of KASH1 disrupts LINC complexes. Fig. S3 characterizes perinuclear actin bundles and shows that they decrease nucleus height and are not induced by confinement in cytochalasin-treated cells and confinement increase NE rupture in HeLa cells. Video 1 shows a time lapse of NE rupture and repair and is related to Fig. 1 A. Video 2 shows a time lapse of NE rupture in DMSO treated cells and is related to Fig. 1 B. Video 3 shows a time lapse of NE rupture in cytoD-treated cells and is related to Fig. 1 B. Video 4 shows a time lapse of NE rupture in blebbistatin-treated cells and is related to Fig. 1 C. Video 5 shows a time lapse of nucleus morphology after addition of blebbistatin and is related to Fig. 3. Video 6 shows a time lapse of NE rupture after DMSO treatment and mechanical cell confinement and is related to Fig. 5 F. Video 7 shows a time lapse of NE rupture after cytoD treatment and mechanical cell confinement and is related to Fig. 5 F.

Acknowledgments

We would like to thank Ryan Johnson in the Biodynamics Lab at the University of California, San Diego, for help with microfabrication and Jan Lammerding's laboratory at Cornell University for the LINC complex constructs. We thank the M.J. Murdoch Charitable Trust for the PerkinElmer spinning-disk microscope used for imaging.

M.W. Hetzer is supported by the National Institutes of Health (grants RO1GM098749 and R01NS096786), the Glenn Family Foundation for Aging Research, the NOMIS Stiftung, the American Cancer Society (award number P30CA014195), and a National Institutes of Health Transformative Research Award. E. Hatch was supported by a postdoctoral fellowship from the American Cancer Society (PF-12-137-01-CSM). The project described was supported by the National Cancer Institute (award number P30CA014118195).

The authors declare no competing financial interests.

Submitted: 15 March 2016
Accepted: 1 September 2016

References

Abràmoff, M.D., P.J. Magalhães, and S.J. Ram. 2004. Image processing with ImageJ. *Biophotonics Intern.* 11:36–42. http://dx.doi.org/http://dx.doi.org/10.1117/1.3589100

Anderson, D.J., J.D. Vargas, J.P. Hsiao, and M.W. Hetzer. 2009. Recruitment of functionally distinct membrane proteins to chromatin mediates nuclear envelope formation in vivo. *J. Cell Biol.* 186:183–191. (published erratum appears in *J. Cell Biol.* 2009. 186:929) http://dx.doi.org/10.1083/jcb.200901106

Beaudouin, J., D. Gerlich, N. Daigle, R. Eils, and J. Ellenberg. 2002. Nuclear envelope breakdown proceeds by microtubule-induced tearing of the lamina. *Cell.* 108:83–96. http://dx.doi.org/10.1016/S0092-8674(01)00627-4

Campeau, E., V.E. Ruhl, F. Rodier, C.L. Smith, B.L. Rahmberg, J.O. Fuss, J. Campisi, P. Yaswen, P.K. Cooper, and P.D. Kaufman. 2009. A versatile viral system for expression and depletion of proteins in mammalian cells. *PLoS One.* 4:e6529. http://dx.doi.org/10.1371/journal.pone.0006529

Chancellor, T.J., J. Lee, C.K. Thodeti, and T. Lele. 2010. Actomyosin tension exerted on the nucleus through nesprin-1 connections influences endothelial cell adhesion, migration, and cyclic strain-induced reorientation. *Biophys. J.* 99:115–123. http://dx.doi.org/10.1016/j.bpj.2010.04.011

Cohen, S., A.R. Behzad, J.B. Carroll, and N. Panté. 2006. Parvoviral nuclear import: bypassing the host nuclear-transport machinery. *J. Gen. Virol.* 87:3209–3213. http://dx.doi.org/10.1099/vir.0.82232-0

Dechat, T., S.A. Adam, P. Taimen, T. Shimi, and R.D. Goldman. 2010. Nuclear lamins. *Cold Spring Harb. Perspect. Biol.* 2:a000547. http://dx.doi.org/10.1101/cshperspect.a000547

Denais, C.M., R.M. Gilbert, P. Isermann, A.L. McGregor, M. te Lindert, B. Weigelin, P.M. Davidson, P. Friedl, K. Wolf, and J. Lammerding. 2016. Nuclear envelope rupture and repair during cancer cell migration. *Science.* 352:353–358. http://dx.doi.org/10.1126/science.aad7297

de Noronha, C.M., M.P. Sherman, H.W. Lin, M.V. Cavrois, R.D. Moir, R.D. Goldman, and W.C. Greene. 2001. Dynamic disruptions in nuclear envelope architecture and integrity induced by HIV-1 Vpr. *Science.* 294:1105–1108. http://dx.doi.org/10.1126/science.1063957

De Vos, W.H., F. Houben, M. Kamps, A. Malhas, F. Verheyen, J. Cox, E.M.M. Manders, V.L.R.M. Verstraeten, M.A.M. van Steensel, C.L.M. Marcelis, et al. 2011. Repetitive disruptions of the nuclear envelope invoke temporary loss of cellular compartmentalization in laminopathies. *Hum. Mol. Genet.* 20:4175–4186. http://dx.doi.org/10.1093/hmg/ddr344

Gruenbaum, Y., and R. Foisner. 2015. Lamins: nuclear intermediate filament proteins with fundamental functions in nuclear mechanics and genome regulation. *Annu. Rev. Biochem.* 84:131–164. http://dx.doi.org/10.1146/annurev-biochem-060614-034115

Gruenbaum, Y., A. Margalit, R.D. Goldman, D.K. Shumaker, and K.L. Wilson. 2005. The nuclear lamina comes of age. *Nat. Rev. Mol. Cell Biol.* 6:21–31. http://dx.doi.org/10.1038/nrm1550

Hatch, E., and M. Hetzer. 2014. Breaching the nuclear envelope in development and disease. *J. Cell Biol.* 205:133–141. http://dx.doi.org/10.1083/jcb.201402003

Hatch, E.M., A.H. Fischer, T.J. Deerinck, and M.W. Hetzer. 2013. Catastrophic nuclear envelope collapse in cancer cell micronuclei. *Cell.* 154:47–60. http://dx.doi.org/10.1016/j.cell.2013.06.007

Hoffman, D.B., C.G. Pearson, T.J. Yen, B.J. Howell, and E.D. Salmon. 2001. Microtubule-dependent changes in assembly of microtubule motor proteins and mitotic spindle checkpoint proteins at PtK1 kinetochores. *Mol. Biol. Cell*. 12:1995–2009. http://dx.doi.org/10.1091/mbc.12.7.1995

Kanellos, G., J. Zhou, H. Patel, R.A. Ridgway, D. Huels, C.B. Gurniak, E. Sandilands, N.O. Carragher, O.J. Sansom, W. Witke, et al. 2015. ADF and Cofilin1 control actin stress fibers, nuclear integrity, and cell survival. *Cell Reports*. 13:1949–1964. http://dx.doi.org/10.1016/j.celrep.2015.10.056

Khatau, S.B., C.M. Hale, P.J. Stewart-Hutchinson, M.S. Patel, C.L. Stewart, P.C. Searson, D. Hodzic, and D. Wirtz. 2009. A perinuclear actin cap regulates nuclear shape. *Proc. Natl. Acad. Sci. USA.* 106:19017–19022. http://dx.doi.org/10.1073/pnas.0908686106

Le Berre, M., J. Aubertin, and M. Piel. 2012. Fine control of nuclear confinement identifies a threshold deformation leading to lamina rupture and induction of specific genes. *Integr. Biol. (Camb).* 4:1406–1414. http://dx.doi.org/10.1039/c2ib20056b

Le Berre, M., E. Zlotek-Zlotkiewicz, D. Bonazzi, F. Lautenschlaeger, and M. Piel. 2014. Methods for two-dimensional cell confinement. *Methods Cell Biol.* 121:213–229. http://dx.doi.org/10.1016/B978-0-12-800281-0.00014-2

Lombardi, M.L., D.E. Jaalouk, C.M. Shanahan, B. Burke, K.J. Roux, and J. Lammerding. 2011. The interaction between nesprins and sun proteins at the nuclear envelope is critical for force transmission between the nucleus and cytoskeleton. *J. Biol. Chem.* 286:26743–26753. http://dx.doi.org/10.1074/jbc.M111.233700

Lovett, D.B., N. Shekhar, J.A. Nickerson, K.J. Roux, and T.P. Lele. 2013. Modulation of nuclear shape by substrate rigidity. *Cell. Mol. Bioeng.* 6:230–238. http://dx.doi.org/10.1007/s12195-013-0270-2

Maciejowski, J., Y. Li, N. Bosco, P.J. Campbell, and T. de Lange. 2015. Chromothripsis and kataegis induced by telomere crisis. *Cell.* 163:1641–1654. http://dx.doi.org/10.1016/j.cell.2015.11.054

Muchir, A., J. Medioni, M. Laluc, C. Massart, T. Arimura, A.J. van der Kooi, I. Desguerre, M. Mayer, X. Ferrer, S. Briault, et al. 2004. Nuclear envelope alterations in fibroblasts from patients with muscular dystrophy, cardiomyopathy, and partial lipodystrophy carrying lamin A/C gene mutations. *Muscle Nerve.* 30:444–450. http://dx.doi.org/10.1002/mus.20122

Raab, M., M. Gentili, H. de Belly, H.R. Thiam, P. Vargas, A.J. Jimenez, F. Lautenschlaeger, R. Voituriez, A.M. Lennon-Duménil, N. Manel, and M. Piel. 2016. ESCRT III repairs nuclear envelope ruptures during cell migration to limit DNA damage and cell death. *Science.* 352:359–362. http://dx.doi.org/10.1126/science.aad7611

Rothballer, A., and U. Kutay. 2013. The diverse functional LINCs of the nuclear envelope to the cytoskeleton and chromatin. *Chromosoma.* 122:415–429. http://dx.doi.org/10.1007/s00412-013-0417-x

Salina, D., K. Bodoor, D.M. Eckley, T.A. Schroer, J.B. Rattner, and B. Burke. 2002. Cytoplasmic dynein as a facilitator of nuclear envelope breakdown. *Cell.* 108:97–107. http://dx.doi.org/10.1016/S0092-8674(01)00628-6

Schmitz, M.H.A., M. Held, V. Janssens, J.R.A. Hutchins, O. Hudecz, E. Ivanova, J. Goris, L. Trinkle-Mulcahy, A.I. Lamond, I. Poser, et al. 2010. Live-cell imaging RNAi screen identifies PP2A-B55alpha and importin-beta1 as key mitotic exit regulators in human cells. *Nat. Cell Biol.* 12:886–893. http://dx.doi.org/10.1038/ncb2092

Shimi, T., K. Pfleghaar, S. Kojima, C.-G. Pack, I. Solovei, A.E. Goldman, S.A. Adam, D.K. Shumaker, M. Kinjo, T. Cremer, and R.D. Goldman. 2008. The A- and B-type nuclear lamin networks: microdomains involved in chromatin organization and transcription. *Genes Dev.* 22:3409–3421. http://dx.doi.org/10.1101/gad.1735208

Starr, D.A., and H.N. Fridolfsson. 2010. Interactions between nuclei and the cytoskeleton are mediated by SUN-KASH nuclear-envelope bridges. *Annu. Rev. Cell Dev. Biol.* 26:421–444. http://dx.doi.org/10.1146/annurev-cellbio-100109-104037

Steigemann, P., C. Wurzenberger, M.H.A. Schmitz, M. Held, J. Guizetti, S. Maar, and D.W. Gerlich. 2009. Aurora B-mediated abscission checkpoint protects against tetraploidization. *Cell.* 136:473–484. http://dx.doi.org/10.1016/j.cell.2008.12.020

Sullivan, T., D. Escalante-Alcalde, H. Bhatt, M. Anver, N. Bhat, K. Nagashima, C.L. Stewart, and B. Burke. 1999. Loss of A-type lamin expression compromises nuclear envelope integrity leading to muscular dystrophy. *J. Cell Biol.* 147:913–920. http://dx.doi.org/10.1083/jcb.147.5.913

Talamas, J.A., and M.W. Hetzer. 2011. POM121 and Sun1 play a role in early steps of interphase NPC assembly. *J. Cell Biol.* 194:27–37. http://dx.doi.org/10.1083/jcb.201012154

Tamiello, C., M.A.F. Kamps, A. van den Wijngaard, V.L.R.M. Verstraeten, F.P.T. Baaijens, J.L.V. Broers, and C.C.V. Bouten. 2013. Soft substrates normalize nuclear morphology and prevent nuclear rupture in fibroblasts from a laminopathy patient with compound heterozygous LMNA mutations. *Nucleus.* 4:61–73. http://dx.doi.org/10.4161/nucl.23388

Thiam, H.-R., P. Vargas, N. Carpi, C.L. Crespo, M. Raab, E. Terriac, M.C. King, J. Jacobelli, A.S. Alberts, T. Stradal, et al. 2016. Perinuclear Arp2/3-driven actin polymerization enables nuclear deformation to facilitate cell migration through complex environments. *Nat. Commun.* 7:10997. http://dx.doi.org/10.1038/ncomms10997

Vargas, J.D., E.M. Hatch, D.J. Anderson, and M.W. Hetzer. 2012. Transient nuclear envelope rupturing during interphase in human cancer cells. *Nucleus.* 3:88–100. http://dx.doi.org/10.4161/nucl.18954

Vergnes, L., M. Péterfy, M.O. Bergo, S.G. Young, and K. Reue. 2004. Lamin B1 is required for mouse development and nuclear integrity. *Proc. Natl. Acad. Sci. USA.* 101:10428–10433. http://dx.doi.org/10.1073/pnas.0401424101

Versaevel, M., T. Grevesse, and S. Gabriele. 2012. Spatial coordination between cell and nuclear shape within micropatterned endothelial cells. *Nat. Commun.* 3:671. http://dx.doi.org/10.1038/ncomms1668

Vigouroux, C., M. Auclair, E. Dubosclard, M. Pouchelet, J. Capeau, J.-C. Courvalin, and B. Buendia. 2001. Nuclear envelope disorganization in fibroblasts from lipodystrophic patients with heterozygous R482Q/W mutations in the lamin A/C gene. *J. Cell Sci.* 114:4459–4468.